Altering Spin Distribution of Tb_2Pc_3 via Molecular Chirality Manipulation

Xin Liao, Emi Minamitani, Tao Xie, Lianzhi Yang, Wenhao Zhang, Svetlana Klyatskaya, Mario Ruben, and Ying-Shuang Fu*

ABSTRACT: Manipulating the chirality of the spin-polarized electronic state is pivotal for understanding many unusual quantum spin phenomena, but it has not been achieved at the single-molecule level. Here, using scanning tunneling microscopy and spectroscopy (STM/STS), we successfully manipulate the chirality of spin distribution in a triple-decker single-molecule magnet tris(phthalocyaninato) bis(terbium(III))(Tb_2Pc_3) , which is evaporated on a Pb(111) substrate via molecular beam epitaxy. The otherwise achiral Tb_2Pc_3 becomes chiral after being embedded into the self-assembled monolayer films of bis(phthalocyaninato) terbium(III) ($TbPc_2$) . The chirality of the spin distribution in Tb_2Pc_3 is manifested via the spatial mapping of its Kondo resonance state from its ligand orbital. Our first-principles calculations revealed that the spin and molecular chirality are associated with a small rotation followed by a structural distortion of the top Pc, consistent with the experimental observation. By constructing tailored molecular clusters with the STM tip, a single Tb_2Pc_3 molecule can be manipulated among achiral and differently handed chiral configurations of spin distributions reversibly. This paves the way for designing chiral spin enantiomers for fundamental studies and developing functional spintronic devices.

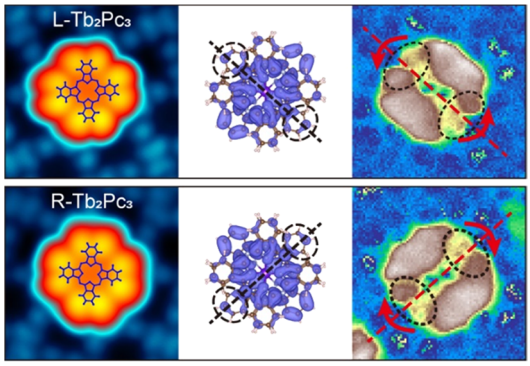

INTRODUCTION

Chirality refers to the geometrical phenomenon of handedness in which two objects are mutual mirror images of each other and, thus, cannot be superimposed onto their counterparts. Chirality plays a pivotal role in several disciplines, such as biorecognitive processes,[1,2] enantioselective chemistry,[3,4] condensed matter, and high-energy physics.[5,6] Notably, the chirality of spin states supports topological magnetic excitations in either the real or reciprocal space, revealing a wealth of emergent quantum phenomena,[7−9] and providing a platform for spintronic applications, where the spin current is generated and reversely acts on the chiral structures for information processing.[10] The intimate connection between chiral structures and spins is explicitly manifested by chirality-induced spin selectivity, which depicts the generation of a spin-polarized current via the flow of electrons through chiral molecules or chiral crystals.[11−14] In this respect, manipulating the chirality of the spin state at the single-molecule level is desirable for elucidating the underlying mechanism behind the interplay between the structural chirality and spin states; however, this has not yet been achieved. Scanning tunneling microscopy and spectroscopy (STM/STS) can be used to characterize and manipulate single molecules with atomic resolution, making it an ideal tool for investigating the chiral distribution of spin states in molecular enantiomers.[15−18]

In this paper, we report the visualization and manipulation of the chirality of the spin distribution hosted in single Tb_2Pc_3 molecules on a Pb(111) substrate. Intermolecular interaction incurs structural chirality in Tb_2Pc_3 molecules via the relative rotation and distortion of their top Pc rings. Structural distortion induces a chiral distribution of the spin states, as can be observed from the Kondo state mapping. Interconversion between achiral and differently handed chiral spin distributions was achieved by constructing tailored molecular clusters composed of single Tb_2Pc_3 and neighboring $TbPc_2$ molecules using STM tip manipulation. This study demonstrates a viable method for manipulating the chiral distribution of spin states at the single-molecule level.

EXPERIMENTAL SECTION

The measurements were performed in a custom-made Unisoku STM system (1300) at 0.4 K under ultrahigh-vacuum conditions.[19] $TbPc_2$ and Tb_2Pc_3 molecules were thermally evaporated from a home-built evaporator at 650−700 K, where Tb_2Pc_3 molecules were formed via a

chemical reaction of the $TbPc_2$ precursors that decomposed into TbPc and Pc in the crucible.[20] The molecules were deposited on the Pb(111) island surface at room temperature and pregrown on a $SrTiO_3$(001) substrate using molecular beam epitaxy. First-principles calculations were conducted using the Vienna ab Initio Simulation Package[21−23] with the projected augmented-wave method. Correction via van der Waals interactions developed by Hamada[24] was used. Detailed methods are described in the Supporting Information.

RESULTS AND DISCUSSION

The triple-decker Tb_2Pc_3 molecule contains two Tb ions sandwiched between three Pc ligands that mutually stack at 45°, whereas the double-decker $TbPc_2$ has a molecular structure similar to that of Tb_2Pc_3 but with one TbPc decker missing [Figure 1(a)]. The $TbPc_2$ molecules self-assemble into

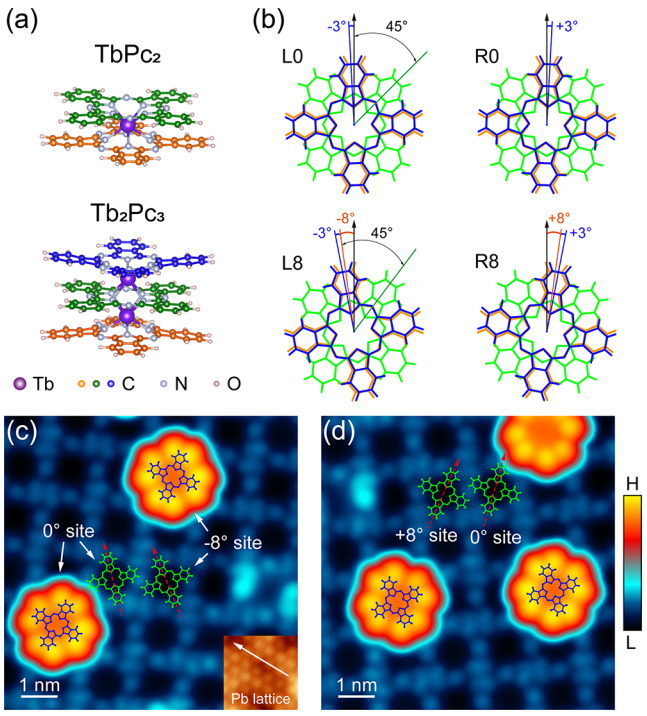

Figure 1. Structure and morphology of $TbPc_2$ and Tb_2Pc_3 on Pb(111). (a) Molecular structures of $TbPc_2$ and Tb_2Pc_3. (b) Top view of the structural models of the four categories of chiral Tb_2Pc_3. The bottom, middle-, and top-layer Pc ligands in (a, b) are labeled in orange, green, and blue, respectively. The black arrow represents the Pb lattice direction. The stacking angles of Pc ligands in different layers are indicated. (c, d) STM images (V = −1.0 V and I = 10 pA) of $TbPc_2$ molecular films embedded with left-handed (right-handed) Tb_2Pc_3 molecules. The structural models of the top Pc ligands are superimposed onto selective $TbPc_2$ and Tb_2Pc_3 molecules, whose occupation sites are labeled. The inset in (c) shows an atomic-resolution image (V = −5.0 mV and I = 40 nA) of the Pb(111) substrate, where one of the Pb lattice directions is marked with a white arrow.

a square lattice upon surface adsorption, with sparsely embedded Tb_2Pc_3 molecules that appear brighter.[18] High-resolution STM images of the molecular film [Figure 1(c,d)] at −1.0 V show the eight-lobed structure of the $TbPc_2$ and Tb_2Pc_3 molecules, which originate from their top Pc ligands.[18,25,26]

An observation of the orientations of the $TbPc_2$ molecules reveals that each $TbPc_2$ molecule rotates by 8° with respect to its nearest neighbors, forming a checkerboard-like pattern. The uncertainty of the determined angle is ±1° (Supporting Note 2). Although the bottom Pc of $TbPc_2$ cannot be directly visualized, its orientation can be inferred from the single Pc and TbPc deckers that originate from the cracked pieces of $TbPc_2$. As shown in Figure S4, single Pc and TbPc deckers were attached to the edges of the $TbPc_2$ films, whose orientations consequently conformed to the bottom Pc of $TbPc_2$. The single Pcs and TbPcs also rotated by 8° relative to their nearest neighbors. This demonstrates that the alternating rotation of $TbPc_2$ occurs at the bottom Pc relative to the Pb lattice and maintains an internal stacking angle of 45° between the top and bottom Pcs. This observation is distinct from previous studies of $TbPc_2$ on Au(111) and Ag(111) surfaces, where two Pc deckers rotated internally in the $TbPc_2$ films.[25,27,28]

By comparing the lattice orientation of the Pb substrate, we deduced that the bottom Pc deckers of $TbPc_2$ either aligned along the Pb lattice, that is, 0°, or were misaligned by 8°. The misalignment angle is designated as −8° (+8°) for the case of counterclockwise (clockwise) rotation relative to the Pb lattice. As such, the molecular sites in the $TbPc_2$ films are labeled as 0, −8, and +8° sites. Within each molecular film, the misaligned angle is of the same type, and thus the films are denoted as −8 and +8° films.

After identifying the stacking configuration of the $TbPc_2$ molecules, we investigated the embedded Tb_2Pc_3 molecules. Although the bottom and middle Pcs of Tb_2Pc_3 cannot be visualized, they are naturally assumed to adopt the same stacking configuration as that of $TbPc_2$ because of their similar molecular structures. This assumption was supported by our first-principles calculations later. The high-resolution STM images in Figure 1(c,d) reveal that the top Pc of Tb_2Pc_3 rotates by an additional −3° (+3°) with respect to its bottom Pc in the −8° (+8°) $TbPc_2$ films. Such an additional rotation renders the otherwise achiral Tb_2Pc_3 molecules structurally chiral. Their two enantiomers are left-handed and right-handed for Tb_2Pc_3 possessing additional rotation angles of −3 and +3°, respectively. Accounting for the occupation sites of Tb_2Pc_3, these molecules are classified into four categories: As shown in Figure 1(b), the Tb_2Pc_3 molecules residing at the 0° and −8° sites (0° and +8° sites) in the −8° (+8°) films are all left-handed (right-handed) and are labeled as L0 and L8 (R0 and R8) Tb_2Pc_3, respectively.

Considering the intimate connection between the molecular structure and spin states, we expect that chiral Tb_2Pc_3 molecules may host chiral spin states. Subsequently, we investigated the chirality of the ligand spins. Note that the f-spin of the Tb ion is too localized to be detected in conventional STM experiments and will not be discussed for simplicity.[25,29] In the gas phase, $TbPc_2$ has an unpaired spin delocalized over its two Pc ligands, in contrast to Tb_2Pc_3, which has no radical spin owing to the complete pair of its π system. Upon adsorption on Pb, the ligand spin states change, and owing to the electron transfer from the substrate, $TbPc_2$ becomes nonmagnetic, whereas Tb_2Pc_3 may acquire a ligand spin. The ligand spin in Tb_2Pc_3 manifests itself as a Kondo resonance in the tunneling spectrum of STM.[18]

To determine the chirality of the ligand spin states, we investigated the spatial distribution pattern of Kondo resonances in Tb_2Pc_3. Figure 2(a−d) shows typical STM images of the four types of Tb_2Pc_3 embedded inside the $TbPc_2$ films. An out-of-plane magnetic field of 2 T was applied to quench the superconductivity of the Pb substrate and avoid

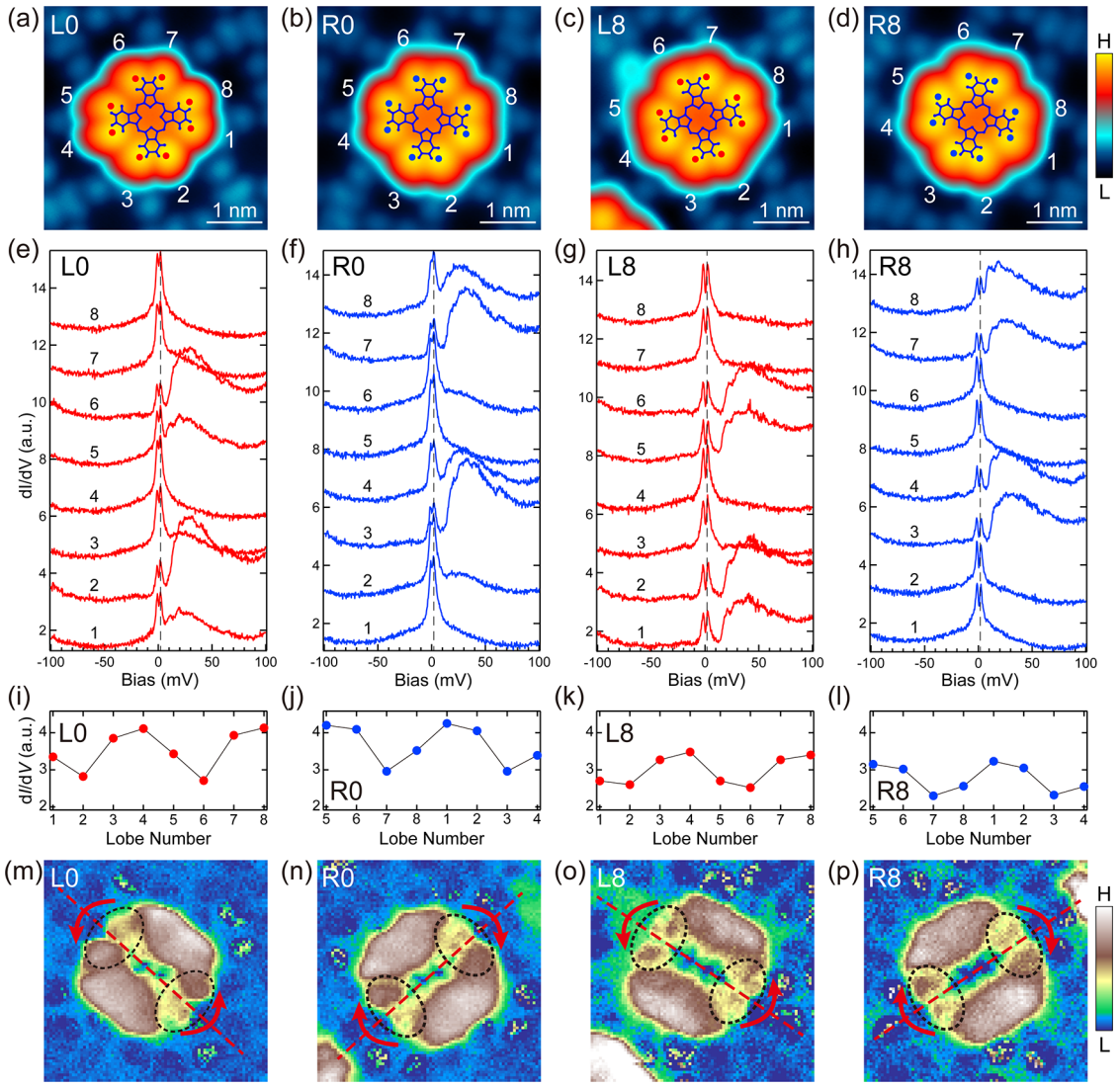

Figure 2. Chiral distribution of spin states in embedded Tb_2Pc_3. (a–d) High-resolution STM images (V = −1.0 V and I = 10 pA) of the four categories of Tb_2Pc_3 molecules (L0, R0, L8, and R8) embedded inside the $TbPc_2$ films. The Pb lattice direction is in the vertical direction. (e, h) Tunneling spectra (V = −100 mV and I = 200 pA, V_{mod} = 1.0 mV) on eight lobes of the L0 (e), R0 (f), L8 (g), and R8 (h) Tb_2Pc_3 molecules under B = 2 T. Spectra were obtained at locations marked by eight red (blue) dots in L0 and L8 (R0 and R8) Tb_2Pc_3 molecules, whose lobe numbers are marked. The dashed lines mark the right peak of the split Kondo peaks at V = 2 mV. The applied magnetic field quenches the superconductivity of the substrate and splits the Kondo peak. The Zeeman splitting energy at 2 T is low, which does not influence the overall spectral shape of the Kondo resonance. (i–l) Variation of the Kondo peak intensity at 2 mV in (e–h), respectively. Note that the sequence of lobe numbers are arranged to reflect the mutual chiral relation of (i, j) and (k, l). (m–p) dI/dV mapping (I = 200 pA, V_{mod} = 2.0 mV) of Tb_2Pc_3 in (a–d) taken at 2 mV under B = 2 T, showing the spatial distribution of the Kondo resonance. The dotted ellipses highlight the chiral distribution of the spin states.

entanglement with the Kondo effect. The tunneling spectra acquired on their eight lobes all showed prominent Kondo resonance peaks [Figure 2(e–h)] but exhibited different intensities in their Kondo peaks. The Kondo peak intensities indicated apparent oscillations against the lobe numbers, which were arranged in the same manner for all four categories of Tb_2Pc_3 [Figure 2(i–l)]. Notably, the oscillatory behavior of the Kondo intensity for the L0 and R0 (L8 and R8) Tb_2Pc_3 molecules was out of phase. In contrast, the oscillations of the L0 and L8 (R0 and R8) Tb_2Pc_3 molecules were in phase. This suggests the existence of a chiral distribution of the Kondo peak intensities and that L0 and L8 Tb_2Pc_3 share the same chiral handedness, which is distinct from that of the R0 and R8 molecules.

The chiral handedness was directly determined from the spatial distribution of the Kondo resonance state obtained through spectroscopy mapping at a Kondo peak energy of 2 mV (Figure 2(m–p)). While the STM images of the Tb_2Pc_3 molecules appear 4-fold symmetric, the symmetry of their Kondo mappings appears *apparently* 2-fold, with apparent symmetric axes (marked with red dashed lines) along the diagonal direction of, instead of along, the top Pc lobes. However, a careful inspection of the Kondo mapping indicates that its apparent 2-fold symmetry is invalid because the two neighboring lobes spanning the apparent symmetric axes exhibit increased conductance intensity in the counterclockwise direction (marked with red arrows) for L0 Tb_2Pc_3 [Figure 2(m)]. In contrast, a clockwise conductance increase was observed for R0 Tb_2Pc_3 [Figure 2(n)]. The same phenomenon of the conductance increase in the counterclockwise (clockwise) direction also occurs in L8 (R8) Tb_2Pc_3 [Figure 2(o,p)]. These observations unambiguously demonstrate the chiral

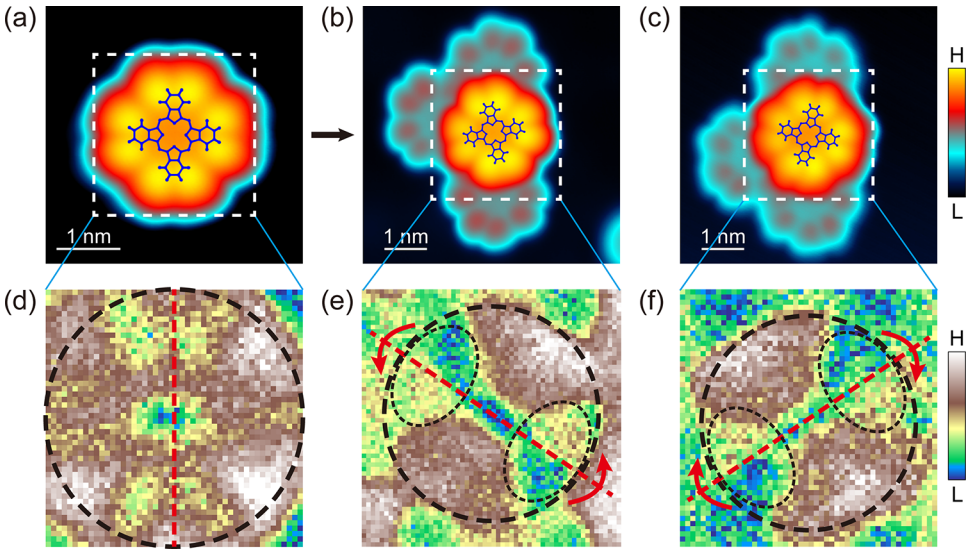

Figure 3. Chirality manipulation of a single Tb_2Pc_3 on Pb(111). (a–c) STM images (V = −1.0 V and I = 10 pA) of an isolated single Tb_2Pc_3 before and after being assembled with neighboring $TbPc_2$. The Pb lattice direction is in the vertical direction. (d–f) dI/dV mapping of the rectangle area in (a–c), taken at 2 mV under B = 2 T. The spatial ranges of the Tb_2Pc_3 are indicated by black dashed circles. The dotted ellipses highlight the chiral distribution of spin states.

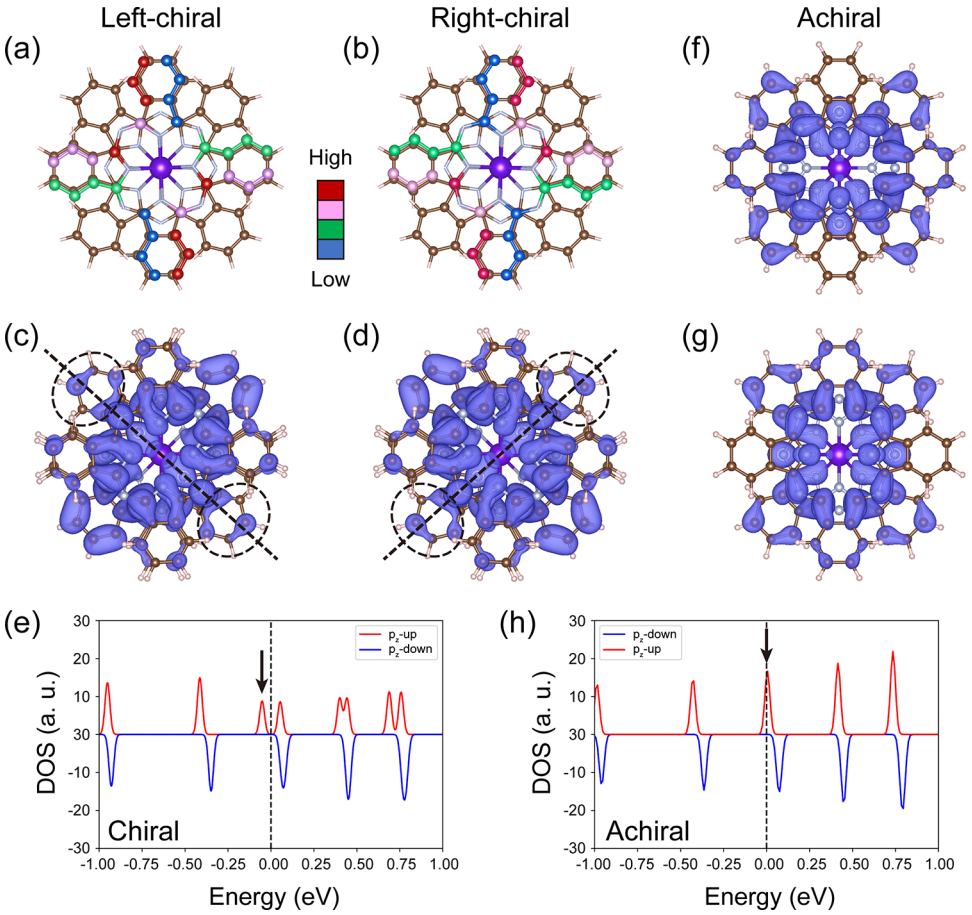

Figure 4. DFT calculations on the chiral distribution of spin states in the $[Tb_2Pc_3]^-$ molecule. (a, b) Structural model of left-chiral (a) and right-chiral (b) $[Tb_2Pc_3]^-$, showing propeller-like structural distortion of C atoms in their top Pc, whose different atomic heights are depicted with colors. (c, d) Charge distributions of the SOMO orbital for left-chiral (c) and right-chiral (d) configurations. These two distributions are chiral to each other, as evident in the regions highlighted by the dotted ellipses. (e) Density of states projected onto C p_z orbitals for the $[Tb_2Pc_3]^-$ molecule in chiral (achiral) configurations. The spin-polarized SOMO orbital, indicated by the black arrow, appears immediately below the Fermi level (0 eV). (f, g) Charge distribution of the doubly degenerate LUMO orbitals for the achiral configuration.

distribution of the Kondo resonance states, which are left-handed in L0 and L8 Tb_2Pc_3 molecules and right-handed in R0 and R8 Tb_2Pc_3 molecules. Note that the symmetric axes of the Kondo mappings in chiral Tb_2Pc_3 have equivalent directions that are orthogonal to each other, as shown in Figure S5.

As the handedness of Tb_2Pc_3 was identical in each $TbPc_2$ film, we inferred that molecular chirality was induced by interactions between Tb_2Pc_3 and its neighboring $TbPc_2$ molecules. To justify this conjecture, we manipulated the embedded Tb_2Pc_3 from the molecular film using the STM tip [Figure S6], rendering the isolated Tb_2Pc_3 devoid of intermolecular interaction. As shown in Figure 3(a), the top Pc of the isolated Tb_2Pc_3 was aligned with the Pb lattice direction (vertical direction), indicating the disappearance of structural chirality, in contrast to the embedded Tb_2Pc_3. Furthermore, the Kondo resonance mapping of isolated Tb_2Pc_3 [Figure 3(d)] shows strict 2-fold symmetry. Interestingly, the symmetric axis of the Kondo mapping changes along the top Pc lobes, which is distinct from the diagonal direction in embedded Tb_2Pc_3. These observations demonstrate that the isolated Tb_2Pc_3 is achiral.

Having identified the role of intermolecular interaction in endowing the molecular chirality, we demonstrated the capability of controlling the chirality of the structural and spin distribution in Tb_2Pc_3 among the achiral and different chiral handedness states in tailored molecular clusters artificially built using STM tip manipulation.[30] Figure 3(b) shows such a molecular tetramer composed of Tb_2Pc_3 with three neighboring $TbPc_2$. Tb_2Pc_3 was of the L8 type, as inferred from its orientation relative to the Pb lattice. Indeed, its Kondo resonance mapping displayed a chiral distribution with left-handedness [Figure 3(e)], conforming to that of embedded L8 Tb_2Pc_3. Similarly, a molecular tetramer in which the orientation of the included Tb_2Pc_3 was determined to be of the R8 type was assembled [Figure 3(c)]. The Kondo state mapping features right-handed chirality, as expected for embedded R8 Tb_2Pc_3 [Figure 3(f)]. Notably, once the molecular clusters are assembled, they tend to move laterally as a whole entity and are difficult to separate by tip manipulation [Figure S7]. This suggests that intermolecular interactions are important. We also constructed other types of molecular clusters composed of Tb_2Pc_3 with one neighboring $TbPc_2$ and two neighboring $TbPc_2$ molecules. Both types of molecular clusters exhibited a chiral distribution of spin states [Figure S8], demonstrating that one neighboring $TbPc_2$ molecule is sufficient to induce molecular chirality.

Although the rotation of the top Pc in Tb_2Pc_3 naturally induces structural chirality in the molecule, it is intriguing to observe a drastic change in the spin distribution of the ligand orbital, considering that the rotation angle of 3° is minute. Density functional theory (DFT) calculations were performed to determine the origin of the chiral spin states of Tb_2Pc_3. As the ligand spin of Tb_2Pc_3 is activated via electron transfer from the substrate,[18] we calculated the free $[Tb_2Pc_3]^-$ state with one excess electron residing at its lowest molecular orbital (LUMO). In accordance with experimental observations, the left (right)-chiral Tb_2Pc_3 was set to have its top Pc rotated by 3° in the counterclockwise (clockwise) direction.

The electron occupation of the LUMO state causes Jahn–Teller distortion after structural optimization, resulting in a propeller-like distortion of the carbon atom coordinates within the topmost Pc ligand (Figure 4(a,b)). The helicity of the propeller was the opposite for left- and right-chiral Tb_2Pc_3. This structural distortion lifted the originally doubly degenerate LUMO [Figure 4(c–e)]. One singly occupied molecular orbital (SOMO) appeared immediately below the Fermi level in both handed configurations, generating ligand spins [Figure 4(e)]. The spin polarization at this SOMO is the origin of the experimental Kondo effect. Indeed, the charge distributions of the SOMO shown in Figure 4(c,d) were consistent with the observed Kondo peak distributions. Specifically, the high-Kondo intensity region in Figure 2(i,j) corresponds to the high charge density at the two opposite lobes of the middle Pc ligand. More importantly, the charge distributions in the other two opposite lobes of the middle Pc ligand (marked with dotted ellipses) exhibited different chiral intensities, which agreed well with the experimental Kondo distribution. In contrast, the chirality of both the structural distortion and the charge intensity distribution disappeared for the Tb_2Pc_3 molecule without rotation. Interestingly, the calculated charge distribution for achiral Tb_2Pc_3 is 2-fold symmetric, whose mirror axis is along the two opposite lobes of the top Pc ligand [Figure 4(f–h)], which is consistent with the experimental Kondo intensity distribution [Figure 3(a)]. These results suggest that the rotation of the top Pc ligand, followed by Jahn–Teller distortion, is the origin of the experimentally observed chiral Kondo peak distribution.

Understanding the mechanisms that drive molecular chirality is essential. To this end, we performed additional DFT calculations based on a freestanding molecular lattice composed of Tb_2Pc_3 with four neighboring $TbPc_2$ molecules. To mimic the influence of the substrate, we added an additional electron to each molecule to reflect the charge transfer from the substrate observed in the experiments. We also fixed the orientation of the bottom Pc for both $TbPc_2$ and Tb_2Pc_3 by using the angle determined from the experiments. The angle between the bottom and middle Pcs in Tb_2Pc_3 was fixed at 45°, and the total energy was evaluated with respect to the angle between the top and bottom Pcs in Tb_2Pc_3. Interestingly, as shown in Figure S9, the total energy in the lattice case reaches its minimum when the top Pc rotates by approximately ±3°. In contrast, the minimum appears at a rotation angle of 0° in the isolated case. This observation is consistent with the experimental results and rigorously demonstrates that intermolecular interaction is the driving force for the induction of molecular chirality in Tb_2Pc_3. Such chirality induction by intermolecular interaction is likely to be extended to other molecular systems.

CONCLUSIONS

We investigated the chiral spin states of Tb_2Pc_3 on the Pb(111) substrates. Upon embedding in the molecular lattice of $TbPc_2$, the originally achiral Tb_2Pc_3 molecules acquire structural chirality, owing to the minute 3° rotation of their top-layer Pc ligands. The chirality of the molecular structure and the spin distribution were determined from high-resolution STM imaging and Kondo resonance state mapping. Our DFT calculations showed that the chiral distribution of the spin states is associated with electron-transfer-induced Jahn–Teller distortion, generating structural chirality in Tb_2Pc_3. Our study identified the role of intermolecular interaction in endowing molecular chirality, which is utilized to tune the chirality of Tb_2Pc_3 among achiral and chiral handedness states controllably in tailored molecular clusters built by tip manipulation. Our study provides a platform for manipulating the chirality of the spin distribution at the single-

molecule level and paves the way for developing spintronic applications based on chiral molecular magnets.

AUTHOR INFORMATION

Corresponding Author

Ying-Shuang Fu − *School of Physics and Wuhan National High Magnetic Field Center, Huazhong University of Science and Technology, Wuhan 430074, China; Wuhan Institute of Quantum Technology, Wuhan 430206, China;* orcid.org/0000-0001-7876-2812; Email: yfu@hust.edu.cn

Authors

Xin Liao − *School of Physics and Wuhan National High Magnetic Field Center, Huazhong University of Science and Technology, Wuhan 430074, China; Wuhan Institute of Quantum Technology, Wuhan 430206, China*

Emi Minamitani − *SANKEN, Osaka University, Ibaraki, Osaka 567-0047, Japan*

Tao Xie − *School of Physics and Wuhan National High Magnetic Field Center, Huazhong University of Science and Technology, Wuhan 430074, China; Wuhan Institute of Quantum Technology, Wuhan 430206, China*

Lianzhi Yang − *School of Physics and Wuhan National High Magnetic Field Center, Huazhong University of Science and Technology, Wuhan 430074, China; Wuhan Institute of Quantum Technology, Wuhan 430206, China*

Wenhao Zhang − *School of Physics and Wuhan National High Magnetic Field Center, Huazhong University of Science and Technology, Wuhan 430074, China; Wuhan Institute of Quantum Technology, Wuhan 430206, China;* orcid.org/0000-0003-2386-0305

Svetlana Klyatskaya − *Institute of Nanotechnology, Karlsruhe Institute of Technology, Eggenstein-Leopoldshafen 76344, Germany*

Mario Ruben − *Institute of Nanotechnology and Institute for Quantum Materials and Technologies, Karlsruhe Institute of Technology, Eggenstein-Leopoldshafen 76344, Germany; Centre Européen de Sciences Quantiques, Institut de Science et d'Ingénierie Supramoléculaires, 67083 Strasbourg, France*

Notes

The authors declare no competing financial interest.

ACKNOWLEDGMENTS

The authors gratefully acknowledge financial support from the National Key Research and Development Program of China (Grant No. 2022YFA1402400) and the National Natural Science Foundation of China (Grant Nos. U20A6002, 92265201, 12174131), and Natural Science Foundation of Hubei (2022CFB033), and Knowledge Innovation Program of Wuhan-Basic Research (2023010201010056). DFT calculations were performed using a computer facility at the Research Center for Computational Science (Okazaki, Japan). S.K. and M.R. gratefully acknowledge financial support from the Deutsche Forschungsgemeinschaft (DFG, German Research Foundation) through the Collaborative Research Centre "4f for Future" (CRC 1573, project number 471424360).

REFERENCES

(1) Sanchez, C.; Arribart, H.; Guille, M. M. G. Biomimetism and bioinspiration as tools for the design of innovative materials and systems. *Nat. Mater.* **2005**, *4* (4), 277−288, DOI: 10.1038/nmat1339.

(2) Harrison, K.; Mackay, A. S.; Kambanis, L.; Maxwell, J. W. C.; Payne, R. J. Synthesis and applications of mirror-image proteins. *Nat. Rev. Chem.* **2023**, *7* (6), 383−404.

(3) Phipps, R. J.; Hamilton, G. L.; Toste, F. D. The progression of chiral anions from concepts to applications in asymmetric catalysis. *Nat. Chem.* **2012**, *4* (8), 603−614.

(4) Gong, W.; Chen, Z.; Dong, J.; Liu, Y.; Cui, Y. Chiral Metal-Organic Frameworks. *Chem. Rev.* **2022**, *122* (9), 9078−9144.

(5) Kamada, K.; Yamamoto, N.; Yang, D.-L. Chiral effects in astrophysics and cosmology. *Prog. Part. Nucl. Phys.* **2023**, *129*, No. 104016, DOI: 10.1016/j.ppnp.2022.104016.

(6) Tokura, Y.; Seki, S.; Nagaosa, N. Multiferroics of spin origin. *Rep. Prog. Phys.* **2014**, *77* (7), No. 076501.

(7) Streubel, R.; Fischer, P.; Kronast, F.; Kravchuk, V. P.; Sheka, D. D.; Gaididei, Y.; Schmidt, O. G.; Makarov, D. Magnetism in curved geometries. *J. Phys. D: Appl. Phys.* **2016**, *49* (36), No. 363001, DOI: 10.1088/0022-3727/49/36/363001.

(8) Tokura, Y.; Kanazawa, N. Magnetic Skyrmion Materials. *Chem. Rev.* **2021**, *121* (5), 2857−2897.

(9) Hasan, M. Z.; Chang, G.; Belopolski, I.; Bian, G.; Xu, S.-Y.; Yin, J.-X. Weyl, Dirac and high-fold chiral fermions in topological quantum matter. *Nat. Rev. Mater.* **2021**, *6* (9), 784−803.

(10) Yang, S.-H.; Naaman, R.; Paltiel, Y.; Parkin, S. S. P. Chiral spintronics. *Nat. Rev. Phys.* **2021**, *3* (5), 328−343.

(11) Göhler, B.; Hamelbeck, V.; Markus, T. Z.; Kettner, M.; Hanne, G. F.; Vager, Z.; Naaman, R.; Zacharias, H. Spin Selectivity in Electron Transmission Through Self-Assembled Monolayers of Double-Stranded DNA. *Science* **2011**, *331* (6019), 894−897.

(12) Naaman, R.; Paltiel, Y.; Waldeck, D. H. Chiral molecules and the electron spin. *Nat. Rev. Chem.* **2019**, *3* (4), 250−260.

(13) Naaman, R.; Waldeck, D. H. Chiral-Induced Spin Selectivity Effect. *J. Phys. Chem. Lett.* **2012**, *3* (16), 2178−2187.

(14) Shitade, A.; Minamitani, E. Geometric spin−orbit coupling and chirality-induced spin selectivity. *New J. Phys.* **2020**, *22* (11), No. 113023, DOI: 10.1088/1367-2630/abc920.

(15) Morgenstern, K. Switching individual molecules by light and electrons: From isomerisation to chirality flip. *Prog. Surf. Sci.* **2011**, *86* (5−8), 115−161.

(16) De Feyter, S.; Gesquière, A.; Abdel-Mottaleb, M. M.; Grim, P. C. M.; De Schryver, F. C.; Meiners, C.; Sieffert, M.; Valiyaveettil, S.; Müllen, K. Scanning Tunneling Microscopy: A Unique Tool in the Study of Chirality, Dynamics, and Reactivity in Physisorbed Organic Monolayers. *Acc. Chem. Res.* **2000**, *33* (8), 520−531.

(17) De Feyter, S.; De Schryver, F. C. Two-dimensional supramolecular self-assembly probed by scanning tunneling microscopy. *Chem. Soc. Rev.* **2003**, *32* (3), 139−150.

(18) Xia, H. N.; Minamitani, E.; Zitko, R.; Liu, Z. Y.; Liao, X.; Cai, M.; Ling, Z. H.; Zhang, W. H.; Klyatskaya, S.; Ruben, M.; Fu, Y. S. Spin-orbital Yu-Shiba-Rusinov states in single Kondo molecular magnet. *Nat. Commun.* **2022**, *13* (1), No. 6388.

(19) Yang, X.; Xian, J.-J.; Li, G.; Nagaosa, N.; Zhang, W.-H.; Qin, L.; Zhang, Z.-M.; Lü, J.-T.; Fu, Y.-S. Possible Phason-Polaron Effect on Purely One-Dimensional Charge Order of Mo6Se6 Nanowires. *Phys. Rev. X* **2020**, *10* (3), No. 031061, DOI: 10.1103/PhysRevX.10.031061.

(20) Hellerstedt, J.; Cahlik, A.; Svec, M.; de la Torre, B.; Moro-Lagares, M.; Chutora, T.; Papouskova, B.; Zoppellaro, G.; Mutombo,

P.; Ruben, M.; et al. On-surface structural and electronic properties of spontaneously formed Tb(2)Pc(3) single molecule magnets. *Nanoscale* **2018**, *10* (33), 15553−15563.
(21) Kresse, G.; Furthmüller, J. Efficient iterative schemes for ab initio total-energy calculations using a plane-wave basis set. *Phys. Rev. B* **1996**, *54* (16), 11169−11186.
(22) Kresse, G.; Furthmüller, J. Efficiency of ab-initio total energy calculations for metals and semiconductors using a plane-wave basis set. *Comput. Mater. Sci.* **1996**, *6* (1), 15−50.
(23) Blöchl, P. E. Projector augmented-wave method. *Phys. Rev. B* **1994**, *50* (24), 17953−17979.
(24) Hamada, I. van der Waals density functional made accurate. *Phys. Rev. B* **2014**, *89* (12), No. 121103(R), DOI: 10.1103/PhysRevB.89.121103.
(25) Komeda, T.; Isshiki, H.; Liu, J.; Zhang, Y. F.; Lorente, N.; Katoh, K.; Breedlove, B. K.; Yamashita, M. Observation and electric current control of a local spin in a single-molecule magnet. *Nat. Commun.* **2011**, *2*, No. 217.
(26) Rizzini, A. L.; Krull, C.; Mugarza, A.; Balashov, T.; Nistor, C.; Piquerel, R.; Klyatskaya, S.; Ruben, M.; Sheverdyaeva, P. M.; Moras, P.; et al. Coupling of single, double, and triple-decker metal-phthalocyanine complexes to ferromagnetic and antiferromagnetic substrates. *Surf. Sci.* **2014**, *630*, 361−374, DOI: 10.1016/j.susc.2014.07.008.
(27) Ara, F.; Qi, Z. K.; Hou, J.; Komeda, T.; Katoh, K.; Yamashita, M. A scanning tunneling microscopy study of the electronic and spin states of bis(phthalocyaninato)terbium(iii) (TbPc(2)) molecules on Ag(111). *Dalton Trans.* **2016**, *45* (42), 16644−16652.
(28) Barhoumi, R.; Amokrane, A.; Klyatskaya, S.; Boero, M.; Ruben, M.; Bucher, J. P. Screening the 4f-electron spin of TbPc(2) single-molecule magnets on metal substrates by ligand channeling. *Nanoscale* **2019**, *11* (44), 21167−21179.
(29) Fu, Y. S.; Schwobel, J.; Hla, S. W.; Dilullo, A.; Hoffmann, G.; Klyatskaya, S.; Ruben, M.; Wiesendanger, R. Reversible chiral switching of bis(phthalocyaninato) terbium(III) on a metal surface. *Nano Lett.* **2012**, *12* (8), 3931−3935.
(30) Amokrane, A.; Klyatskaya, S.; Boero, M.; Ruben, M.; Bucher, J.-P. Role of π-Radicals in the Spin Connectivity of Clusters and Networks of Tb Double-Decker Single Molecule Magnets. *ACS Nano* **2017**, *11* (11), 10750−10760.